Available online at www.sciencedirect.com
SCIENCE DIRECT®
ELSEVIER
Nuclear Physics A 723 (2003) 229–248
NUCLEAR PHYSICS A
www.elsevier.com/locate/npe

Classical drop phase diagram and correlations in phase space

A. Chernomoretz *, P. Balenzuela, C.O. Dorso

Departamento de Física, Facultad de Ciencias Exactas y Naturales, Universidad de Buenos Aires, Pabellón 1 Ciudad Universitaria, 1428 Buenos Aires, Argentina

Received 24 December 2002; received in revised form 13 March 2003; accepted 18 March 2003

Abstract

The phase diagram of a finite, constrained, and classical system is built from the analysis of cluster distributions in phase and configurational spaces. According to the calculated critical exponents τ, and γ, three regions can be identified. One (low density limit) in which first order phase transition features can be observed. Another one, corresponding to the high density regime, in which fragments in phase space display critical behavior of 3D-Ising universality class type. An intermediate density region, in which power-laws are displayed but cannot be associated to the abovementioned universality class, can also be recognized.

PACS: 25.70.-z; 25.70.Mn; 25.70.Pq; 02.70.Ns

Keywords: Finite system; Phase transitions; Clusters; Multifragmentation

1. Introduction

The multifragmentation phenomenon that takes place in nuclei with excitation energies above 2 MeV/nucleon has been one of the central issues of the nuclear community during the past two decades. In particular, one feature that triggered the interest on the field was the important detected production of intermediate mass fragments (IMF's). Excited nuclei break up in many IMF's in Fermi energy range reactions. This feature, along with the fact that early calculations of caloric curves showed an approximately constant behavior for

* Corresponding author.
E-mail address: ariel@df.uba.ar (A. Chernomoretz).

0375-9474/03/$ – see front matter
doi:10.1016/S0375-9474(03)01230-2

a given range of excitation energies, was interpreted by many groups as a signature of a phase transition taking place in finite nuclear systems [1–5].

In recent contributions the behavior of the microcanonical heat capacity was used to experimentally characterize the transition as a first order one [6]. Within this picture, the latent heat can be associated with the transformation between a Fermi liquid and a gas phase, composed by light particles and free nucleons.

The familiar liquid-gas transition framework seems to be appropriate to deal with the nuclear case. However one key point usually disregarded is that by its own nature multifragmentation in nuclear reactions should be a priori analyzed as a non-equilibrium process [7,8]. In spite of this remark a global equilibrium scenario is usually adopted by the experimental nuclear community. In particular, statistical models of the MMMS [9] or SMM [10] type, that modelize the fragmenting system as an ideal gas of non-interacting clusters in the spirit of Fisher theory, are widespreadly used to analyzed experimental data.[1]

The working hypothesis usually made by such models is that a freeze-out volume can be defined inside of which the existence of an equilibrated ensemble of clusters can be assumed. In this approach, the behavior of thermodynamic quantities is closely related to the way the system is *partitionated* into clusters (isolated drops) giving rise to internal surfaces.

In this contribution we want to explore in detail the fragmentation scenario assumed by these statistical models. To that end, we use molecular dynamics (MD) techniques to sample the microcanonical ensemble associated with confined fragmenting systems that interacts via a two-body Lennard–Jones potential. The analogy between the nuclear force and the van der Waals interaction supports the use of this simplified classical model to obtain qualitatively meaningful results.

Given the MD microcanonical description, the pressure and temperature can be estimated from the generalized equipartition theorem [11], whereas the specific heat can be related to kinetic energy fluctuations [12]. On the other hand, a complementary analysis of the microscopic correlations at a particle level of description can also be considered. To that end, different fragment-recognition algorithms can be used in order to unveil different particle–particle correlation properties. In this way, we are able to obtain caloric curves (CC) which resemble the ones obtained within the statistical approach (that includes a vapor branch), but in addition we can use the available microscopic information to better understand the observed behavior.

Inhomogeneities and surfaces are to be carefully considered in the study of finite systems [13]. We focus our attention on the consequences that the constraining volume imposes to the appearance of well defined internal surfaces. While statistical models assume the existence of an equilibrated ensemble of already formed and well defined fragments in configurational space at fragmentation, this is not the case within our approach. We use different cluster definitions that consider correlations in different spaces to relate the internal surfaces suppression, as density is increased, with the appearance of critical signals in phase-space defined cluster distributions.

[1] Through the present contribution, all this models in which the corresponding configurations are built from a Monte Carlo kind of sampling compatible with a given distribution function will be referred as *statistical models*.

Previous studies [15–17] have already dealt with this 'cluster structure-thermodynamic description' mapping. They made used of Hill's cluster definition [18] , and were mainly focused on the system behavior in the supercritical phase ($\rho > \rho_c, T > T_c$), where a percolation-like line of critical points was observed.

In this contribution we consider two alternative fragment definitions that, at variance with Hill's clusters (that in the present paper will be called MSTE clusters, as will be explained in Section 3), are built in well defined and physically meaningful spaces. The first one, associated with the so-called minimum spanning tree fragment recognition method, is based on configurational information (MST clusters). The second one uses complete phase space information in order to define a fragment set according to the most bound density fluctuation in phase space [19] (ECRA clusters).

Using this fragment characterization as a fundamental piece of information, consistent phase diagrams are built taking into account exact microscopic information in both, energy-density, and temperature-density planes. In addition, we can identify a noticeable property of scale-free mass distributions for ECRA clusters: a balance between intra-cluster and inter-cluster potential interaction can be observed whenever power-law distributions are obtained (see Fig. 8).

This paper is organized as follows. In Section 2 we will describe the model used in our simulations. Section 3 is devoted to a characterization of the used cluster definitions. A description of expected signals associated with phase transitions in finite systems is given in Section 4. In Section 5 the study of the phase diagram is presented. Finally, conclusions are drawn in Section 6.

2. The model

The system under study is composed by excited drops made up of 147 particles interacting via a 6–12 Lennard Jones potential, which reads:

$$V(r) = \begin{cases} 4\epsilon\left[\left(\frac{\sigma}{r}\right)^{12} - \left(\frac{\sigma}{r}\right)^{6} - \left(\frac{\sigma}{r_c}\right)^{12} + \left(\frac{\sigma}{r_c}\right)^{6}\right] r \leqslant r_c, \\ 0 r > r_c. \end{cases} \tag{1}$$

We took the cut-off radius as $r_c = 3\sigma$. Energies are measured in units of the potential well (ϵ), and σ is taken as the distance unit. The unit of time used is: $t_0 = \sqrt{\sigma^2 m/48\epsilon}$.

In order to constrain the dynamics we used a spherical confining 'wall'. The considered external potential behaves like $V_{\text{wall}} \sim (r - r_{\text{wall}})^{-12}$ with a cut off distance $r_{\text{cut}} = 1\sigma$, where it smoothly became zero along with its first derivative. The set of classical equations of motion were integrated using the well-known velocity Verlet algorithm [20]. Initial conditions were constructed from a ground state configuration by assigning velocities from a Maxwell–Boltzmann distribution in order to attain the desired total energy value. Once the transient behavior was over, a microcanonical sampling of particle configurations every $5t_0$ up to a final time of $140000t_0$ was performed.

3. Fragment definitions

The simplest and more intuitive cluster definition is based on correlations in configuration space: a particle i belongs to a cluster C if there is another particle j that belongs to C and $|\mathbf{r_i} - \mathbf{r_j}| \leqslant r_{\mathrm{cl}}$, where r_{cl} is a parameter called the clusterization radius. We set $r_{\mathrm{cl}} = r_c = 3\sigma$.

The algorithm that recognizes these clusters is known as "minimum spanning tree" (MST). In this method only correlations in **q**-space are used, neglecting completely the effect of momentum. As was shown in Ref. [21], in the context of expanding finite systems, MST clusters give incorrect information about the meaningful fragment structure for dense configurations. However, an interesting point to be notice is that it can still provide useful information about the limit imposed by the constraining finite volume to the formation of well defined fragments in configurational space. As $r_{\mathrm{cl}} = r_c$, no inter-cluster interaction exists for MST aggregates, so cluster surfaces can be univocally defined.

An extension of the MST is the "minimum spanning tree in energy space" (MSTE) algorithm [18]. In this case, a given set of particles $i, j, \ldots, k$, belongs to the same cluster C_i if:

$$\forall i \epsilon\, C_i, \quad \exists j \epsilon C_i / e_{ij} \leqslant 0 \tag{2}$$

where $e_{ij} = V(r_{ij}) + (\mathbf{p}_i - \mathbf{p}_j)^2/4\mu$, and μ is the reduced mass of the pair $\{i, j\}$.

The MSTE algorithm searches for configurational correlations between particles considering the relative momenta of particle pairs, and typically recognizes fragments earlier than MST in highly excited unconstrained systems [21,22]. Moreover, in Ref. [23] it has been shown that this cluster definition is equivalent to the clusterization prescription adopted by Coniglio and Klein to define physically meaningful clusters in lattice-gas systems [24].

Finally, a more robust cluster definition is based on the system "most bound density fluctuation" (MBDF) in phase space [19]. The MBDF is composed by the set of clusters $\{C_i\}$ for which the sum, $E_{\{C_i\}}$, of the fragment internal energies attains its minimum value:

$$E_{\{C_i\}} = \sum_i E_{\mathrm{int}}^{C_i} \quad \text{with } E_{\mathrm{int}}^{C_i} = \sum_{j \in C_i} K_j^{\mathrm{cm}} + \sum_{\substack{j,k \in C_i \\ j \leqslant k}} V_{j,k}. \tag{3}$$

K_j^{cm} is the kinetic energy of particle j measured in the center of mass frame of the cluster which contains particle j, and V_{ij} stands for the inter-particle potential.

The algorithm that finds the MBDF is known as the "early cluster recognition algorithm" (ECRA). It searches for simultaneously well correlated structures in both, **q**, and **p** space, via the minimization of the potential and the kinetic terms of Eq. (3).

The ECRA algorithm has been used extensively in many studies of free expanding fragmenting systems [7,25] and has helped to discover that excited drops break very early in the evolution. In addition, in a recent contribution [8] it was shown that ECRA clusters are also suitable to describe the fragmentation transition that takes place in volume constrained systems.

4. Characterizing the transition

As mentioned in the introduction, several observables can be studied in order to analyze phase transitions phenomena occurring in finite systems. They usually involve the behavior of caloric curves [1,4,26–29], specific heats [6,30], kinetic energy fluctuations [5,14], fragment mass distributions [31], and critical exponents [32].

4.1. Thermodynamical description

One of the most relevant quantities in the study of fragmenting systems, either constrained or free to expand, is the caloric curve (CC). The CC is defined as the functional relationship between the system energy and its temperature, given by:

$$T(E) = \frac{2}{3(N-1)} \langle K \rangle_E \tag{4}$$

being N the number of particles, and $\langle K \rangle_E$ the mean kinetic energy averaged over a fixed total energy MD simulation.[2]

In Fig. 1(a) CC's are shown for the following densities: $\rho^h = 0.55\sigma^{-3}$, $\rho^c = 0.35\sigma^{-3}$, $\rho^m = 0.07\sigma^{-3}$, and $\rho^l = 0.01\sigma^{-3}$.

Different behaviors can be recognized. For the more diluted case, ρ^l (full triangles), the corresponding CC displays a loop which ends in a linearly increasing temperature line which we refer as *vapor branch*. Taking into account that within the microcanonical ensemble the specific heat is defined as:

$$\frac{1}{C} = \frac{\partial T}{\partial E} = -T^2 \frac{\partial^2 S}{\partial E^2} \tag{5}$$

it is clear that for this case negative values of C between two poles will be found in the range $0.1\epsilon_0 < E < 0.6\epsilon_0$. A negative value of the derivative of the temperature as a function of the energy reflects an 'anomalous' behavior of the system entropy for the respective energy range. A *convex intruder* in $S(E)$, prohibited in the thermodynamical limit, arises as a consequence of the finiteness of the system and the corresponding lack of extensivity of thermodynamical quantities like S. This signal is expected in first order phase transitions, and is associated to a negative branch of the heat capacity between two poles [8,13]. In addition, as kinetic energy fluctuations and the system specific heat are related by [33]:

$$\frac{1}{N} \left\langle (\delta K)^2 \right\rangle_E = \frac{3}{2\beta^2} \left(1 - \frac{3}{2C} \right) \tag{6}$$

negative values of the specific heat appear whenever $(\delta K)^2$ gets larger than the corresponding canonical expectation value: $\frac{3N}{2\beta^2}$. This behavior has already been verified in Ref. [8].

[2] It should be noticed that, when dealing with unconstrained expanding systems, the quantities appearing in Eq. (4) should be calculated at the time of fragment formation (see [7]).

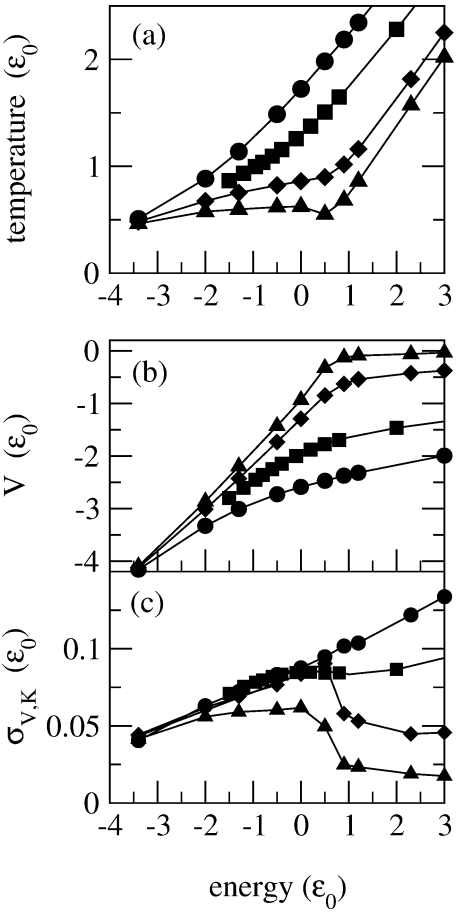

Fig. 1. The caloric curve is shown in panel (a). In panels (b) and (c) the potential energy (V) and its root mean squared deviation as a function of the system total energy are displayed in panels (b) and (c), respectively. The following density values: $\rho = 0.01, 0.07, 0.35,$ and $0.55\sigma^{-3}$, displayed with full triangles, diamonds, squares, and circles, respectively, were considered.

As the density is increased the loop is washed away and it is replaced by an inflection point (ρ^m, full diamonds in Fig. 1(a)). This corresponds to the merging of the specific heat poles into a single local maximum. Finally, for higher densities, ρ^c and ρ^h (filled diamonds, and circles), no major changes in the CC's second derivative can be observed.

In Fig. 1(b) the mean potential energy per particle, V, as a function of the total system energy is displayed. For the lowest densities (triangles and diamonds) two different regimes can be recognized. For $E < 0.5\epsilon_0$ V increases steeply. This can be related to an increase of the mean inter-particle distance, the appearance of internal surfaces, and the corresponding increase of the number of well defined fragments, as the number of attractive bonds decreases. For higher energies, $E > 0.5\epsilon_0$, a saturating behavior can be observed. For

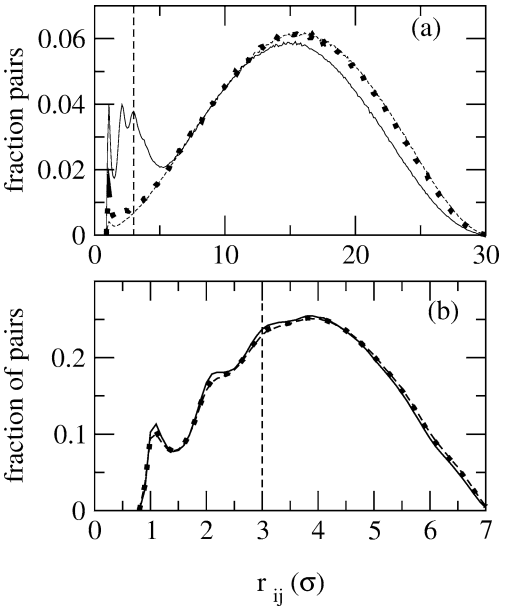

Fig. 2. Normalized inter-particle distance distribution calculated for $\rho^l = 0.01\sigma^{-3}$ and $\rho^h = 0.8\sigma^{-3}$ systems are shown in panels (a) and (b), respectively. The following three total energy values, $E = 0.0, 0.5, 1.0\epsilon_0$, were considered in panel (a), whereas $E = -0.50, 0.5, 1.0\epsilon_0$ for panel (b). They are shown with, solid, dotted, and dashed lines, respectively. Note the different scales used for r_{ij} in both panels.

denser systems, no such feature can be observed. A smooth behavior is displayed by V, instead.

Another interesting feature can be noticed looking at the root mean square deviation of partial energies (kinetic or potential), $\sigma_{V,K}$, shown in Fig. 1(c). For the lowest densities (filled triangles and diamonds) an abrupt decrease is observed at $E \sim 0.5\epsilon_0$, whereas for the highest considered density, $\rho^h = 0.8\sigma^{-3}$(filled circles), no trace of such behavior can be reported. For future reference, it is worth noting that the transition in the monotonic character of the curve takes place at a density value $\rho \sim \rho^c = 0.35\epsilon_0$(filled squares).

To attain a better understanding of the behavior of the magnitudes displayed in Fig. 1(b) and (c), we have followed two strategies: (i) to study particle–particle spatial correlations, (ii) to analyze fragment mass distributions according to the already presented fragment definitions. In what follows we present results obtained within the first approach, and postpone to the next subsection the analysis of fragment distribution properties.

In Fig. 2 the distribution of inter-particle distances, r_{ij}, is shown. Two density values already considered in Fig. 1, namely, ρ^l and ρ^h, are shown in panels (a) and (b), respectively.

For each density, three total energy values [lower than (solid line), equal to (dotted line), and larger than (dashed line) $E = 0.5\epsilon_0$] were considered (see caption). In both panels, a vertical line was included indicating the interaction cut-off radius.

In panel (a) (very diluted case) a well defined structure of interacting particle pairs can be seen at low energies (continuous line). The displayed peaks signal the presence of

a rather large self-sustained drop with a first, second and even third nearest neighbors structure (a bell-shaped distribution, associated with the 'trivial' non-interacting pair counting can also be noticed). As energy increases, this structure fades away, and an important reduction of the number of interacting particles can be recognized. This occurs as a consequence of the spacious volume available, that is big enough to accommodate small non-interacting aggregates. In this transition, well defined **q**-space clusters appear, surfaces are produced and V tends towards a residual value (see bellow).

A completely different behavior is observed for the denser case, ρ^h, shown in Fig. 2(b). In this case, no changes in the statistical distribution of r_{ij} is observed as the energy is increased. (Note that in this case the bell-shaped distribution is superimposed over the peak structure as a consequence of the reduced available volume. However, the presence of a first, second, and even a third nearest neighbors can still be traced). The container imposes a severe volume restriction on the system, and even for high total energy values, each particle is confined in the attractive range of partners potential, between the repulsive core of nearest neighbors.

This last observation completes the general picture within which the behavior of the mean potential energy, V, for high density cases can be understood. As more energy is added to the system no structural transition is allowed by the constraining volume. Particles cannot escape from neighbors most attractive potential range and a smooth increased in V, related to the average time spent in the most negative potential regions, can be seen (Fig. 1(b)).

The decreasing behavior of σ_V, observed for low densities (filled triangles, and diamonds in Fig. 1(c)), can be associated with the loss of 'attractive bonds' between particle pairs that takes place when a non-interacting light cluster regime dominates. As an increasing number of particles stop interacting with one another, the system dynamics gets 'less chaotic' (see [34] for a dynamical characterization of this system), and a strong decrease of σ_V is induced.

This is not the case for higher densities. Each particle is always *connected* to every other system particle through a path of strongly interacting neighbors. Therefore, an increase of the fluctuations in potential energy between successive configurations as total energy is added can be expected (see the behavior displayed by σ_V in Fig. 1(c)).

It is worth noting that the presented picture can also be used to interpret recent results regarding the behavior of the maximum Lyapunov exponent, MLE, in constrained systems. Moreover, a striking similitude between the behavior of $\sigma_V(E, \rho)$ and $MLE(E, \rho)$ can be noticed, comparing Fig. 1(c), and Fig. 5 of Ref. [34].

4.2. Fragments inside the volume

In Section 3, three fragment recognition algorithms were described. Each one makes use of different correlation information in order to gather particles into clusters, and then give different physical information about the morphological characteristics of the system under study.

In Fig. 3 the results of the MST algorithm analysis are shown. MST spectra were calculated for different energies ($E = 0.0, 0.5$, and $1.0\epsilon_0$, displayed as full, dotted and

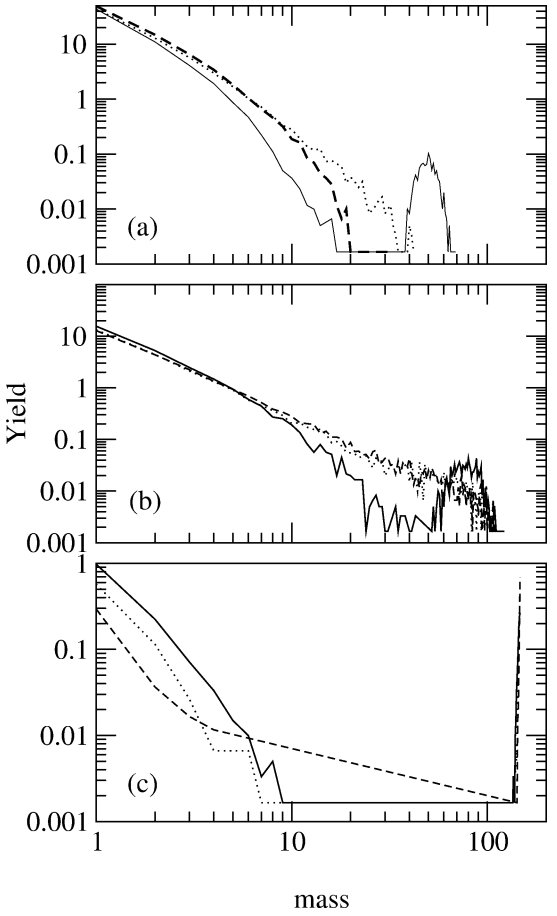

Fig. 3. MST cluster mass distributions calculated for densities: $\rho = 0.01, 0.03$, and $0.10\sigma^{-3}$ are displayed in panels (a), (b), and (c), respectively. Three total energy values were considered for each density, $E_{\mathrm{tot}} = 0.0\epsilon_0, 0.5\epsilon_0$, and $1.0\epsilon_0$. They are displayed as full, dotted and dashed lines, respectively.

dashed lines respectively) for three system densities: $\rho = 0.01, 0.03$, and $0.10\sigma^{-3}$. They are shown in panels (a), (b), and (c), of Fig. 3, respectively.

At low densities, panel 3(a), the system evolves from heavy cluster dominated partitions at low energies, towards a light cluster dominated behavior, at high energies. This reflects the fact that the constraining volume is large enough to allow the system to fragment into well defined drops as energy is increased. It is interesting to notice that results displayed in Fig. 3(a) correspond to full triangle symbols in Fig. 1(a), i.e., the one for which the CC displays a loop. It was argued that big fluctuations in kinetic energy should be expected. This is indeed the case and it is related to the fact that well defined surfaces appear in the system (see [8]).

On the other hand, for denser systems [panels (b), and (c)], it can be noticed that MST size spectra become insensitive to the system energy value once a given volume-dependent

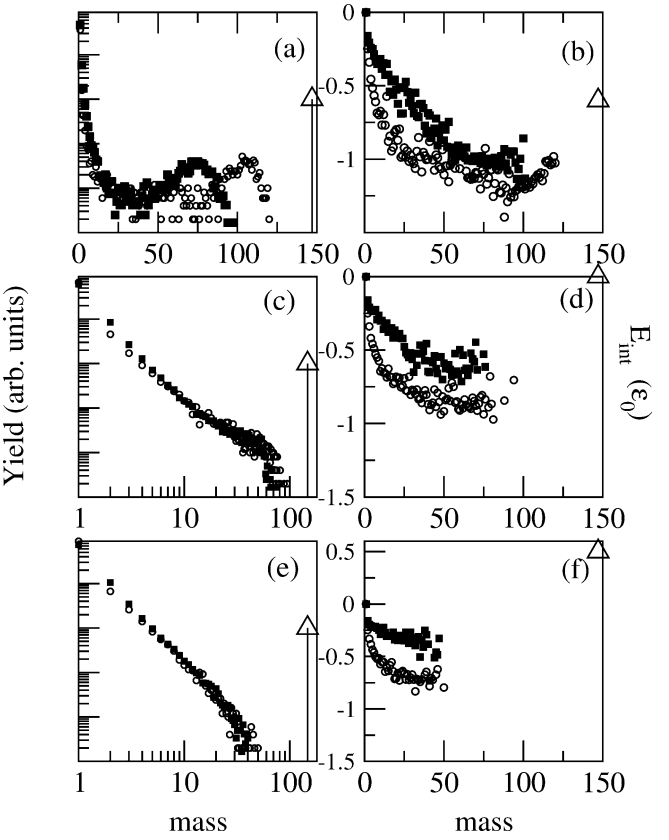

Fig. 4. Fragment mass distribution, and cluster internal energy values as a function of the cluster mass, are shown in the first and second columns, respectively. Three system total energies are considered: $E_{\mathrm{tot}} = -0.6\epsilon_0$, [panels (a), (b)], $0.0\epsilon_0$, [panels (c), (d)], and $0.5\epsilon_0$, [panels (e), (f)]. Empty circles, filled squares, and empty triangles, correspond to ECRA, MSTE, and MST data, respectively.

energy value is achieved. In particular, for $\rho = 0.1\sigma^{-3}$, the mass distributions converge to a u-shaped one no matter the system energy value. Almost no spatially well separated structures (i.e., MST clusters) can be identified in this case, aside from the trivial huge cluster that comprises almost all the system particles.

In Fig. 4, the effect of taking into account momentum correlations in the definition of clusters can be appreciated. A cluster analysis for a system of $N = 147$ particles with $\rho = 0.2\sigma^{-3}$ using ECRA, MSTE, and MST prescriptions is presented in that figure. The mass distribution function, and the fragment internal energy as a function of the cluster mass, $E_{\mathrm{int}}(s)$ (see, Eq. (3)), are shown in the first and second columns, respectively. Three total energy values were considered: $E_{\mathrm{tot}} = -0.6\epsilon_0$ (panels (a), (b)), $0.0\epsilon_0$ (panels (c), (d)), and $0.5\epsilon_0$ (panels (e), (f)). Empty triangles, solid squares, and empty circles correspond to MST, MSTE, and ECRA results, respectively.

It can be seen that, for this density, the MST prescription finds just a big drop. On the other hand, both, the MSTE and ECRA algorithms, find non-trivial cluster distributions

that show the expected transition as the system energy is increased. Even though the mass spectra are qualitatively similar, as a general rule ECRA algorithm produces more bound clusters than the MSTE one. This is consistent with the claim that the MBDF are found by the ECRA algorithm. Due to this feature, from now on, only the properties of the system according to its ECRA cluster structure will be considered.

4.3. Transition signals

As can be seen in Fig. 4 for a $\rho = 0.2\sigma^{-3}$ system, the ECRA cluster distributions undergo a transition from a U-shaped spectrum towards an exponentially decaying one, as energy is increased. Moreover, the mass-distribution corresponding to the intermediate energy value 4(b), displays a power law like behavior. In fact, for *any other* studied density, the same behavior can be reported, and a total energy value can be determined for which a power-law like mass distribution can be found for ECRA fragments.

This result is interesting because it implies that some kind of transition between two regimes, one with, and other without large ECRA drops (i.e., with or without the presence of liquid-like structures in phase space) is taking place even in high density systems. This transition cannot be detected simply using spatial correlations information. Only considering the appropriate cluster prescription power-law-like mass distributions can be used to trace the transition line associated to morphological changes taking place in phase space.

At this point it is worth noting the following remark. It has already been shown that for this kind of system scaling arguments can be applied to ECRA-fragment mass distributions [35,36]. Consequently the following scaling hypothesis can be adopted:

$$n(A) = q_0(\tau)A^{-\tau} f(z), \quad \text{with } z = \epsilon A^{\sigma} \tag{7}$$

$n(A)$ is the number of fragments with mass number A, q_0 is a normalization constant, $f(z)$ is the so-called scaling function. z is the scaling variable, whereas $\epsilon = E_c - E$ is the distance to the critical point E_c. The scaling function has the following properties: it has only one maximum, for $z < 0$, and $f(0) = 1$. Finally, τ, and σ are two critical exponents introduced by the scaling assumption.

According to Eq. (7), at the critical point (i.e., for $\rho \sim \rho_c$, and $E \sim E_c$) the fragment mass distribution can be described by:

$$n(A) = q_0(\tau)A^{-\tau}. \tag{8}$$

Although Eq. (8) is expected to be valid only in the proximity of the critical point, it has been reported [29,37,38] that several critical signatures also appear when first order phase transition are analyzed in finite systems. In particular, as stated in Ref. [38], in small systems the largest cluster gets a size comparable to the vapor fraction before dissapearing when the system crosses the coexistence line. Therefore, there is an energy for which a pseudo-invariance of scale and a resemblance with critical behavior can be expected for small systems undergoing phase transitions that, in the thermodynamical limit, would be univocally classified as first order ones.

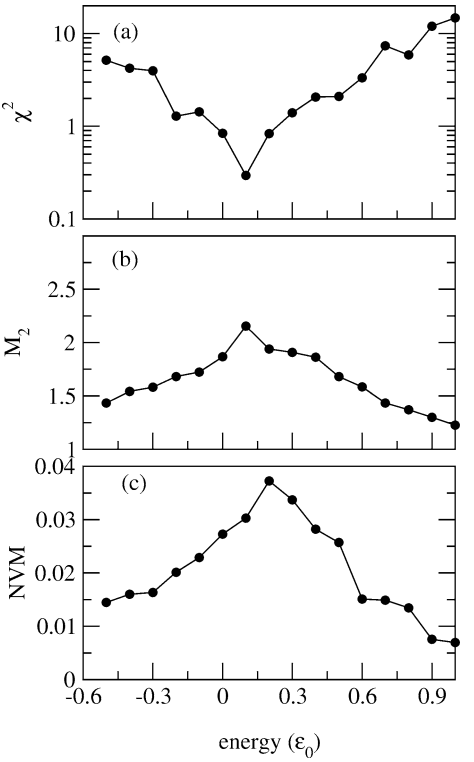

Fig. 5. Transition signatures calculated for a $\rho = 0.10\sigma^{-3}$ system. The χ^2 fitting coefficient, the second moment of the mass distribution, M_2, and the normalized mean variance of the largest fragment, NVM, are displayed in panels (a), (b), and (c), respectively.

Keeping this in mind, given a confining volume, we search for a power-law distribution of ECRA-fragments using the following single parameter function to fit the mass spectra (the contribution of the largest fragment was disregarded) [39]:

$$n(A) = q_0(\tau)A^{-\tau}, \quad \text{with } q_0(\tau) = \frac{1}{\sum_A A^{1-\tau}} \tag{9}$$

$n(A)$ is the number of fragments with mass number A, and q_0 is a normalization constant.

The quality of the fitting procedure was quantified using the standard χ^2 coefficient (see [36] for details), and an energy value, E_*, was associated to the best fitted spectra. In Fig. 5(a) a typical result for χ^2 calculation is shown for ECRA clusters in a $\rho = 0.10\sigma^{-3}$ system. From the figure, a value of $E_* = 0.10 \pm 0.05\epsilon_0$, can be reported.

Another useful observable to search for scale-free distribution functions is the second moment of the cluster distribution $M_2 = \sum'_A A^2 n(A)$. As in the determination of τ, the largest cluster is excluded from the primed sum. M_2 presents a power-law singularity at a second order transition in the thermodynamical limit. For a finite system the divergence is replaced by a maximum. In panel 5(b) the estimation of $M_2(E)$ is shown for a $\rho = 0.10\sigma^{-3}$

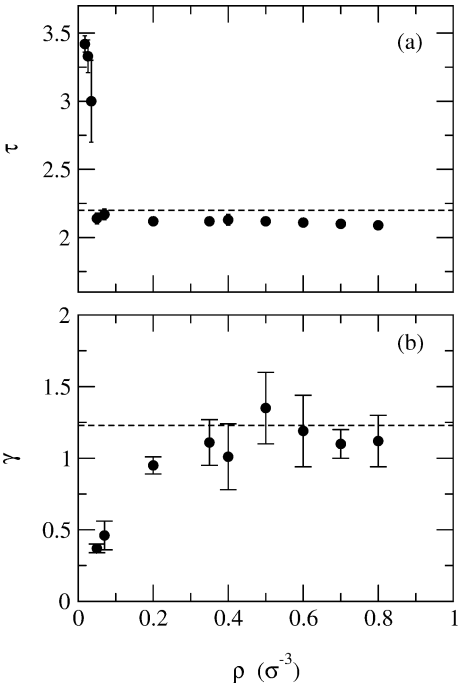

Fig. 6. Estimated values from ECRA cluster distributions for the critical exponents τ and γ are shown in panels (a), and (b), respectively. The expected values for the 3D-Ising universality class are displayed by a dashed line.

system. It can be noticed that the maximum is located at the energy value for which the spectra is best fitted by a power-law like dependence.

This kind of agreement is also achieved when the normalized mean variance, NVM, of the largest fragment mass, $A_{\max}$, is analyzed. NVM is defined as:

$$\mathrm{NVM} = \frac{\langle A_{\max}^2 \rangle - \langle A_{\max} \rangle^2}{\langle A_{\max} \rangle} \tag{10}$$

and it turned out to be a robust tool in the characterization of transition phenomena in which an enhancement of fluctuations occurs [40]. As can be seen from panel 5(c), this signal, although slightly shifted within the working resolution, also peaks in the same region of the previous ones.

The signal agreement reported for the $\rho = 0.10\sigma^{-3}$ case in Fig. 5, is also achieved for every other density analyzed in this paper. This means that in the whole density range power-law mass distributions for phase space defined ECRA clusters are found whenever large fluctuations take place in the system.

In order to properly characterize the state of the system which displays power-law mass distributions, the values attained by the τ exponents must be analyzed as a function of the density. This dependence is shown in Fig. 6(a). For a true critical phenomenon taking place in three-dimensional systems, $2 \leqslant \tau \leqslant 3$ is expected [41]. This condition is not satisfied for systems with $\rho < 0.05\sigma^{-3}$. For these highly diluted systems, the observed free-scale

distribution is not expected to survive the thermodynamic limit. It is not related to any continuous transition, but arises as a finite-size effect. It is worth noting that $\rho \sim 0.05\sigma^{-3}$ is the maximum density for which the respective caloric curve displays a loop, and then, negative c_v (see Fig. 1).

On the other hand, for $\rho > 0.05$, the calculated τ exponents show a rather good agreement with the $\tau = 2.21$ value (dashed line), expected for liquid-gas transitions.

In a second order phase transition, the behavior of M_2 near a critical point can be described in terms of the critical exponent γ [32]:

$$M_2(\epsilon) \propto |\epsilon|^{-\gamma}, \tag{11}$$

where, $\epsilon = Ec - E$, measures the distance to the critical point. This relation is valid for an infinite system in the limit $\epsilon \to 0$. As already mentioned, in a finite system M_2 displays a maximum instead of the divergence predicted in Eq. (11). Having this in mind, a calculation procedure introduced in Refs. [39,42] (*γ-matching*), that takes care of finite size effects, was used to calculate the γ exponent value for our system (see also Ref. [36] for details).

The results of the γ exponent estimation is shown in Fig. 6(b). As density is increased, the obtained values tends toward $\gamma_{\text{liq-gas}} = 1.23$ (dashed line) value that is expected for a liquid-gas transition. It is worth noting that this convergence is achieved for densities $\rho \geqslant 0.35\epsilon_0$ (this value equals ρ^c in Fig. 1). For this density, a change in the behavior of the potential energy fluctuations as a function of the total energy was reported in Fig. 1(c). This can be associated (see Section 4.1) to the onset of the invariance of the statistical interparticle distance distribution (Fig. 2), that takes place as a consequence of the imposed volume restriction.

5. Phase diagram

In the previous section several signatures of a change in the properties of ECRA fragment mass distributions were analyzed. At any given density, a system energy, $E_*(\rho)$, can be determined for which large fluctuations appear in the system, and a scale-free like mass distribution are found.

In Fig. 7, the dependence of E_* with the system density is shown. For $\rho \geqslant 0.35\sigma^{-3}$, a rather constant value is attained for the transition energy. A similar result was reported in Ref. [43], using the already presented MSTE cluster definition.

Some insight about the properties of the system along the line depicted in Fig. 7, can be gained from the analysis of the interplay between the mean internal potential energy per particle stored in ECRA clusters, V_{int}, and the mean inter-cluster interaction energy, V_{ic}.

$$V_{\text{int}} = \sum_{\substack{i<j \\ i,j\in C_k}} V_{i,j}, \tag{12}$$

$$V_{\text{ic}} = \sum_{\substack{i\in C_k,\, j\in C_l \\ k\neq l}} V_{i,j} \tag{13}$$

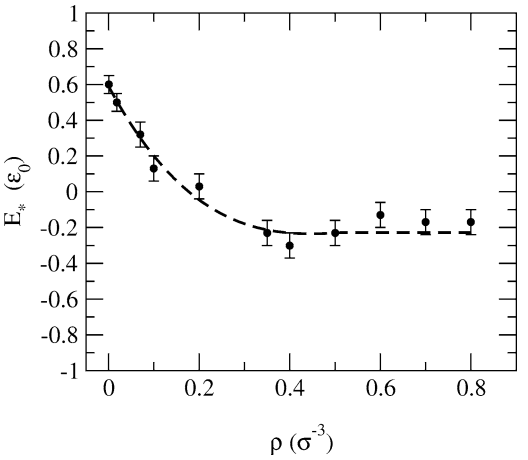

Fig. 7. Density dependence of the system energy, E_*, at which transition signals are detected. The dashed line is included to guide the eye.

V_{int} stands for the mean potential felt by a particle in a cluster due to its interaction with the other members of the same cluster. On the other hand, V_{ic} represents the mean interaction potential felt by a particle due to its interactions with particles belonging to the other clusters. This magnitudes are displayed in Fig. 8 for densities $\rho = 0.01, 0.20, 0.50$, and $0.80\sigma^{-3}$ in panels (a) to (d) respectively.

The general trend displayed by V_{int} and V_{ic} is easy to understand. At any given density, for low energies, a big ECRA cluster can be found having a large binding energy. In addition, as no many other clusters beside the biggest one exist, $V_{\text{ic}} \sim 0$. At high energies, the ECRA partitions turns out to present a rather high multiplicity of light clusters. Consequently $V_{\text{int}} \to 0$ in this limit and V_{ic} absolute value increases.

After a close inspection of Fig. 8, one can realize that for any given density the energy at which $V_{\text{int}} = V_{\text{ic}}$, happens to be $E_*(\rho)$, i.e., the energy at which power-law like mass distributions appear. This means that scale-free ECRA mass distributions have the following property: a balance is established between the mean potential energy that a particle, which belongs to a given cluster, feels due to its interaction with other members of the same cluster and the one associated with its interaction with the rest of the particles in the system. This potential energy balance, that does not allow to distinguish contributions from inside or outside of a cluster, is reminiscent of the vanishment of the chemical potential and surface tension terms that takes place at the critical point.

Given that in this work we have considered a microcanonical description, each sampled event has well defined values of E, V and N. That is why the 'natural' phase diagram to consider should be the one shown in Fig. 7. However, gathering all the information obtained so far, the most usual $T - \rho$ phase diagram can also be built for our 147-particle Lennard–Jones drop (see Fig. 9). The empty circles are (T_*, ρ) points obtained from the aforementioned cluster analysis. The full line is an estimation of the coexistence line, as obtained from the analysis of the system specific heat, c_v (see Eq. (6)). In this case, for densities for which the respective CC displays a loop, $T(E_*)$ has been taken as the average

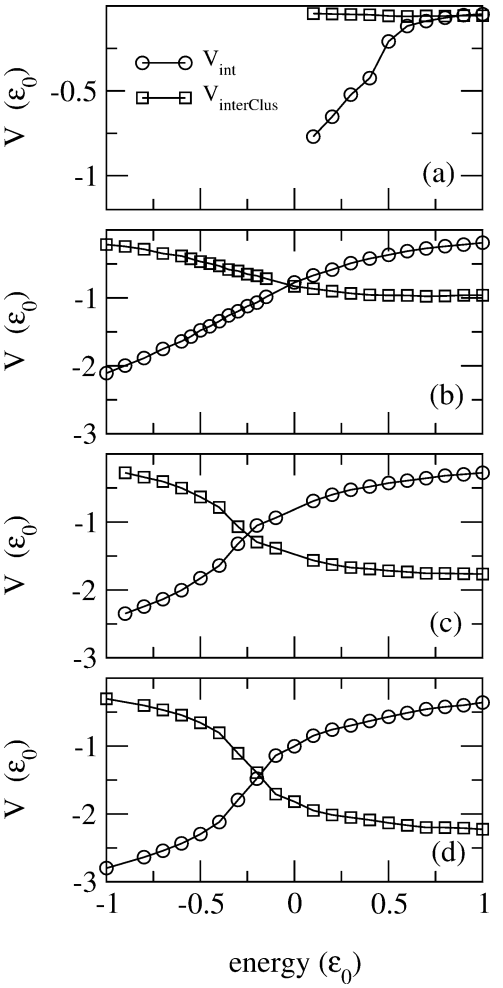

Fig. 8. V_{int} (empty circles) and V_{ic} (empty squares) as a function of the system total energy are shown. Densities: $\rho = 0.01, 0.20, 0.50$, and $0.80\sigma^{-3}$ are displayed in panels (a), (b), (c), and (d), respectively.

temperature between the two values corresponding to the location of the c_v singularities. For denser cases, the location of the maximum of the c_v has been taken. No reliable estimation of the energy that maximizes c_v could be achieved for $\rho > 0.1\sigma^{-3}$ (neither from the CC, nor from the kinetic energy fluctuation behavior).

It should be emphasized that, as in the considered ensemble of events the system volume was not allow to fluctuate, we could not probe the full *thermodynamical* coexistence line. However, it is interesting to notice that from a *strictly morphological* point of view, in phase space, the curve shown in Fig. 9 acts as an effective 'transition line'. For every density value, below this line, a big ECRA structure can be identified, whereas a vapor behavior can be observed above it.

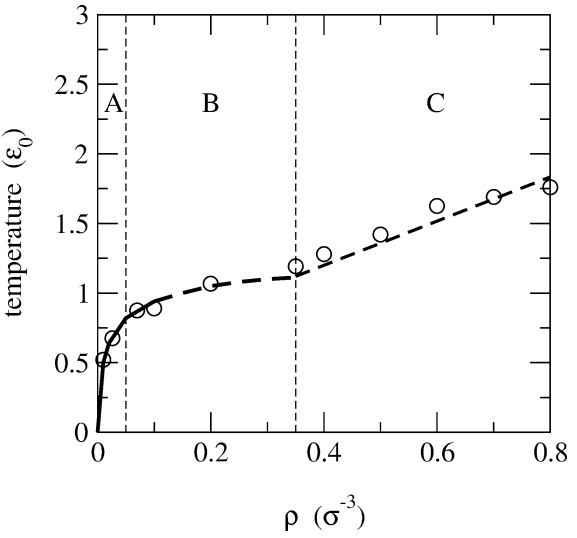

Fig. 9. Phase diagram for a 147 particle Lennard Jones drop. Cluster-based and c_v-based determination of the phase-space transition line is marked with empty circles, and full line, respectively. The dashed line is included to guide the eye.

Moreover, according to the obtained critical exponent values, three density regions can be defined. The region labelled *A* ($\rho \leqslant 0.05\sigma^{-3}$) presents the signals expected for a first order phase transition occurring in a finite system: the corresponding caloric curve shows a loop that can be associated to a negative specific heat, and a structural transition can be recognized (Fig. 2(a)). This region is the only one in which the available volume is large enough for the system to fragment into a set of non-overlapping drops.

On the other hand, in region *C* ($\rho > 0.35\sigma^{-3}$), where the system is rather compressed, and MST algorithm recognizes just one big fragment, a second order transition seems to occur in phase space, whenever the line of critical points is crossed. No anomaly in the respective caloric curve is observed, no qualitative changes in the configuration statistical properties is reported (Fig. 2(b)), and the calculated critical exponents, τ, and γ, are in good agreement with 3D-Ising (liquid-gas) universality class. In addition, it should be noticed that the observed line of *morphological* critical points converges to the *thermodynamical* critical point, approximately located at $\rho_c \sim 0.35\sigma^{-3}$, $T_c \sim 1.1\epsilon$ [43,44].

In between these two regions, region *B* ($0.05\sigma^{-3} < \rho < 0.35\sigma^{-3}$) can be identified. The finite size of the system plays a major role in this density range. Even a sensible τ value suggests that physically meaningful scaling properties are present in the system, the corresponding γ exponent values are too low to classify the transition as a continuous one.

Due to the multivariate nature of the temperature's energy dependence (i.e., the presence of a loop in the respective CC's) that takes place in region A, the following warning should be raised. For this density range, it is not longer valid that ECRA liquid-like structures (U-shaped mass spectra) can only be found bellow the transition line shown in the (T, ρ) plane. The smooth and 'monotonic' character displayed by the mass spectra transition as a function of the system total energy, is lost when T is used as a control parameter. In

this way, for highly diluted finite systems, only in the (E, ρ), (Fig. 7), and not in (T, ρ) plane, the localization of scale-free mass distribution configurations can unambiguously be associated to a meaningful transition line. This peculiarity disappears for more dense situations, region B, and C.

6. Conclusions

In this paper we have undertaken the analysis of thermodynamical and morphological properties of a finite classical system confined in a fixed volume. Apart from the basic interest on such a problem, it is relevant on the frame of the description of fragmenting system according to statistical models.

We have been able to find that the equation of state of such a system is quite simple *from a coordinate-space point of view*. There is a maximum value of the density ($\rho \sim 0.05\sigma^{-3}$) up to which the system fragments into non-interacting drops. In this region the associated CC displays a loop and the thermal response function attains a negative value. For higher densities, there is simply no enough room to allow the system to develop well defined internal surfaces, i.e. only one big drop can be detected. Indeed, with the sharp volume constraint considered in this contribution, the CC or kinetic energy fluctuations are not well suited to recognize the coexistence line for densities greater than $\rho \sim 0.1\sigma^{-3}$.

When one consider a description in which fragments are defined through correlations in **qp**-space, a much richer behavior appears. Now, even for densities bigger than $\rho \sim 0.05\sigma^{-3}$, transitions from u-shaped mass spectra to exponentially decaying ones are signaled by the appearance of scale-free mass distribution of ECRA clusters. From the analysis of critical exponents, τ and γ, related to the displayed power-law distribution, a further classification in density ranges can be obtained. In the abovedefined region A (Section 5), the obtained τ values are too big to be related to a true critical behavior. For densities in the range $0.05\sigma^{-3} < \rho < 0.35\sigma^{-3}$ (region B), even though the τ exponent values are in good agreement with the corresponding 3D-Ising universality class, the value attained by γ critical exponents came out to be too low. Finally, for densities above $\rho \sim 0.35\sigma^{-3}$ (region C), both, τ and γ, are quite close to the accepted values for the 3D-Ising universality class.

Gathering the information obtained so far the following picture emerges. In region A thermodynamical and morphological transitions take place at the same temperature for a given density. Besides, the phase transition can be characterized as a first order one according to the schema proposed by Gross and collaborators [13]. In region B the restriction imposed by the available volume eliminates the abnormal behavior of the caloric curve and the kinetic energy fluctuations (of course, this also occurs in region C). On the other hand, even though a morphological transition line can be identified using phase-space information (ECRA cluster distributions), the corresponding critical exponent values do not agree with the liquid-gas universality class. As a consequence of this, if only information from the NVE ensemble is considered in the description, the transition cannot be cast neither as a first order, nor as a second order one. Finally, in region C, we could identify a morphological coexistence line of critical points of the liquid-gas universality class, starting from the expected thermodynamical critical point.

This is of particular interest for the statistical model approach because by definition, at freeze out, an ensemble of well defined fragments is to be constructed. Such assumption implicitly locates the system under study in region A. It is then clear that in the frame of such approaches regions B and C are excluded from the analysis.

In addition, our microscopic approach allows us to bring some light about the observation of power laws out of the thermodynamical critical point. The crossing of the ECRA inter-cluster and intra-cluster mean potential energies (Fig. 8) turns out to be a very generic feature, related to the existence of large fluctuations and scale-free fragment distributions. This raises at least some warnings against an automatic association between power-laws and the localization of thermodynamical critical points.

Finally, it is worth noting that ECRA clusters are more bound structures than MSTE ones for a given system energy and density (see Fig. 4). This result means that a direct interpretation of MSTE fragments as primordial aggregates is to be taken with care. Specially when such clusters are deexcitated with secondary deexcitation routines to make quantitative comparisons with nuclear experiments.

A natural continuation of this work is to analyze the relation between fragmentation inside the container volume and the corresponding asymptotic mass spectra when walls are removed. This work is currently under progress.

Acknowledgements

The authors wish to thank Francesca Gulimelli and Jean Richert for a careful reading of the manuscript. This work was done with partial financial supports from UBA grant X139. A.Ch. and P.B. are fellow of CONICET. C.O.D is a member of the Carrera de Investigator of CONICET.

References

[1] J. P ochodzalla, et al., Phys. Rev. Lett. 75 (1995) 1040.
[2] V. Serfling, et al., Phys. Rev. Lett. 80 (1998) 3928.
[3] A. Bonasera, M. Bruno, C.O. Dorso, P.F. Mastinu, Rivista Nuovo Cimento 23 (2000) 2;
J. Lopez, C.O. Dorso, Phase Transformations in Nuclear Matter, World Scientific, Singapore, 2000.
[4] D.H.E. Gross, Phys. Rep. 279 (1997) 119.
[5] F. Gulminelli, P. Chomaz, V. Duflot, Europhys. Lett. 50 (4) (2000) 434.
[6] M. D'Agostino, et al., Phys. Lett. B 473 (2000) 219.
[7] A. Strachan, C.O. Dorso, Phys. Rev. C 55 (2) (1997) 775.
[8] A. Chernomoretz, M. Ison, S. Ortiz, C.O. Dorso, Phys. Rev. C 64 (2001) 024606.
[9] D.H. Gross, Rep. Prog. Phys. 53 (1990) 205.
[10] J.B. Bondorf, A.S. Botvina, A.S. Iljinov, I.N. Mishustin, K. Sneppen, Phys. Rep. 257 (1995) 133.
[11] T. Cagin, J.R. Ray, Phys. Rev. A 37 (1988) 247.
[12] J.L. Lebowitz, J.K. Percus, L. Verlet, Phys. Rev. 153 (1967) 250.
[13] D.H.E. Gross, Microcanonical Thermodynamics, World Scientific, Singapore, 2001.
[14] P. Chomaz, F. Gulminelli, Nucl. Phys. A 647 (1999) 153.
[15] X. Campi, H. Krivine, N. Sator, Nucl. Phys. A 681 (2001) 458.
[16] X. Campi, H. Krivine, N. Sator, Physica A 296 (2001) 24.
[17] N. Sator, cond-mat/0210566.

[18] T.L. Hill, J. Chem. Phys. 23 (1955) 617.
[19] C.O. Dorso, J. Randrup, Phys. Lett. B 301 (1993) 328.
[20] D. Frenkel, B. Smit, Understanding Molecular Simulation, From Algorithms to Applications, Academic Press, San Diego, 1996.
[21] A. Strachan, C.O. Dorso, Phys. Rev. C 56 (1997) 1.
[22] A. Chernomoretz, C.O. Dorso, J. López, Phys. Rev. C 64 (2001) 044605.
[23] X. Campi, H. Krivine, Nucl. Phys. A 620 (1997) 46.
[24] A. Coniglio, W. Klein, J. Phys. A: Math. Gen. 13 (1980) 2775.
[25] A. Strachan, C.O. Dorso, Phys. Rev. C 58 (1998) R632;
A. Strachan, C.O. Dorso, Phys. Rev. C 59 (1999) 285;
A. Barrañón, A. Chernomoretz, C.O. Dorso, J. López, J. Morales, Rev. Mexicana Fís. (Suppl. 2) 45 (1999) 110.
[26] J. Pochodzalla, Prog. Part. Nucl. Phys. 39 (1997) 443.
[27] R.M. Lynden-Bell, D.J. Wales, J. Chem. Phys. 101 (2) (1994) 1460.
[28] D.J. Wales, R.S. Berry, Phys. Rev. Lett. 73 (1994) 2875.
[29] J.M. Carmona, N. Michel, J. Richert, P. Wagner, Phys. Rev. C 61 (2000) 037304.
[30] M. Schmidt, R. Kusche, T. Hippler, J. Donges, J. Kronmuller, B. von Issendorff, H. Haberland, Phys. Rev. Lett. 86 (2001) 1191.
[31] J.E. Finn, et al., Phys. Rev. Lett. 49 (1982) 1321.
[32] J.B. Elliott, et al., Phys. Rev. C 62 (2000) 64603.
[33] J.L. Lebowitz, J.K. Percus, J. Verlet, Phys. Rev. 153 (1967) 150.
[34] M. Ison, P. Balenzuela, A. Bonasera, C.O. Dorso, Eur. Phys. J. A 14 (2002) 451.
[35] P. Balenzuela, Ph.D. Thesis, University of Buenos Aires (2002).
[36] P. Balenzuela, A. Chernomoretz, C.O. Dorso, Phys. Rev. C 66 (2002) 024613.
[37] J. Pan, S. Das Gupta, M. Grant, Phys. Rev. Lett 80 (1998) 1182.
[38] F. Gulminelli, P. Chomaz, Int. J. Mod. Phys. E 8 (6) (1999) 527.
[39] H. Nakanishi, H.E. Stanley, Phys. Rev. B 22 (1980) 2466.
[40] C.O. Dorso, V. Latora, A. Bonasera, Phys. Rev. C 60 (1999) 034606.
[41] M.E. Fisher, Rep. Prog. Phys. 30 (1969) 615.
[42] J.B. Elliott, et al., Phys. Rev. C 55 (1997) 1319.
[43] X. Campi, H. Krivine, N. Sator, Cris 2000 3rd Catania Relativistic Ion Studies, Acicastello, Italy (2000).
[44] N. Wilding, Phys. Rev. E 52 (1995) 602.